# Modelling and Simulation of a Novel Bioinspired Flapping-Wing Rotary MAV

Xun Huang, Cranfield University, Cranfield, United Kingdom
Linghai Lu, Cranfield University, Cranfield, United Kingdom
James Whidborne, Cranfield University, Cranfield, United Kingdom
Shijun Guo, Cranfield University, Cranfield, United Kingdom

**Abstract**

Achieving high lift efficiency represents a major research focus in the Micro Air Vehicle (MAV) domain due to stringent size and payload constraints. The Cranfield research team presents a novel semi-biomimetic design called the Flapping Wing Rotor (FWR) to address this challenge. This innovative concept combines a bio-inspired flapping wing mechanism with passive rotor rotation, leveraging unsteady aerodynamic principles analogous to insect flight. The research aims to highlight a promising biomimetic flapping-rotor MAV enabled through advanced modeling to unlock the benefits of bio-inspired unsteady aerodynamics. To demonstrate this approach, a 60g proof-of-concept prototype was developed alongside a digital twin methodology for modeling, simulation, and control. A mathematical model has been formulated to analyze FWR's lift generation performance and enable flight control system design for stabilization and controllability. This work concentrates on enhancing the physical modeling process. The model is refined by tuning two key aerodynamic coefficients to account for nonlinearities from unsteady aerodynamics, flexible structures, and low Reynolds number flow inherent in MAV flight. This improved model achieves superior lift prediction accuracy versus real flight test data. Ongoing efforts focus on optimizing control torque, load distribution, and stability to further augment FWR's flight capabilities.

**List of Symbols**

| | |
|---|---|
| $^{earth}a$ | Body coordinate system acceleration, $m/s^2$ |
| $a_n$ | Acceleration of reference point,mm |
| $c(r)$ | Chord length in location $r$,mm |
| $c_{rot}$ | Rotational force cooeficient |
| $C_{l_{max}}$ | Maximum lift coefficient |
| $\bar{C}_l$ | Average lift coefficient |
| $C_y$ | Y-axis force coefficient |
| $C_z$ | Z-axis force coefficient |
| $dX$ | Force component along the blade elements x axis,N |
| $dZ$ | Force component along the blade elements z axis,N |
| $dF_{rot\_x\_bl}$ | Rotation Force on $x_{bl}$,N |
| $dF_{rot\_z\_bl}$ | Rotation Force on $z_{bl}$,N |
| $dF_{A\_z\_bl}$ | Added mass forces on $z_{bl}$,N |
| $dT$ | The component of aerodynamic force along the $z_{bl}$ axis,N |
| $dQ$ | The component of aerodynamic force along the $x_{bl}$ axis,N |
| $dT_h$ | Component of dT in the hub coordinate system,N |
| $dH_h$ | Backward force in hub coordinate system,N |
| $dS_h$ | Lateral force in hub coordinate system,N |

| | |
|---|---|
| $dM_{kh}$ | Torque in hub coordinate system,N |
| $f$ | Flapping frequency(Hz) |
| $I$ | Inertia matrix of FWR MAV |
| $m$ | Mass of FWR MAV, g |
| ${}^{body}M$ | The monent in body coordinates,N |
| $r$ | Blade element location along spanwise $r$,mm |
| $Re$ | Reynolds number |
| $T$ | Total thrust of the propeller disc,N |
| $t$ | Time in the flapping cycle,s |
| $V_{\infty hub}$ | Relative flow velocity of the hub coordinate system,m/s |
| $W_x$,$W_y$,$W_z$ | Incoming flow velocity in the x, y, and z directions of the blade element coordinate system,m/s |
| $xyz_{earth}$ | Ground coordinate system |
| $xyz_{body}$ | body coordinate system |
| $xyz_{hub}$ | hub coordinate system |
| $\alpha_*$ | The effective AoA,deg |
| $\beta_{AMP}$ | Flapping amplitude,deg |
| $\theta$ | Pitch angle,deg |
| $v_\beta$ | Flapping velocity,m/s |
| $\phi$ | Roll angle,deg |
| $\varphi$ | Pitching angle,deg |
| $\varphi_u$ | Maximum pitch angle,deg |
| $\varphi_d$ | Minimum pitch angle,deg |
| $\chi$ | Angle of the flapping plane,deg |
| $\psi$ | Yaw angle,deg |
| $\Omega$ | Rotor angular velocity,rad/s |
| ${}^{body}\omega$ | Body coordinate system angular velocity, rad/s |
| $\Delta T$ | Dimensionless wing pitch times of dragonflies,s |

**List of Acronyms**

| | |
|---|---|
| AoA | Angle of Attack |
| ERF | European Rotorcraft Forum |
| FWR | Flapping Wing Rotor |
| HF | Horizontal Flapping |
| IF | Inclined Flapping |
| MAV | Micro Air Vehicle |
| RMSE | Root Mean Squared Error |

## 1. INTRODUCTION

Currently, most biomimetic micro air vehicle (MAV) designs worldwide rely on artificially complex mechanical structures to simulate the multi-degree-of-freedom flapping of biological wings. However, this approach of mimicking insect wing kinematics that have evolved over millennia has proven to be remarkably inefficient. Statistics show that the average payload capacity for flapping wing MAVs with less than 50cm wingspan globally is only 16.54 g(Ref.1–Ref.5).

To enhance the mechanical efficiency and payload capacity of biomimetic micro air vehicles (MAVs), the Cranfield bionics research team has pioneered a novel semi-biomimetic MAV concept called the Flapping Wing Rotor (FWR)(Ref.6– Ref.8)(Ref.10). This innovative design embraces a bio-inspired flapping wing actuation strategy, utilizing the flapping thrust to initiate passive rotation of the rotor. By effectively harnessing unsteady aerodynamic phenomena observed in insect flight, including delayed stall and the Weis-Fogh mechanism, and incorporating these into the passive rotor kinematics, exceptional lift generation is achieved(Ref.8).

Recent studies conducted in 2021 demonstrate that compared to conventional flapping wing platforms like the DelFly, the FWR produces over three times more lift under the same 28 cm wingspan(Ref.11). This substantial augmentation stems from the FWR's unique merging of flapping-induced unsteady mechanisms with rotational lift components. This work highlights the promise of selective bio-inspiration targeted at fundamental fluid physics rather than solely morphological mimicry. By distilling the underlying aerodynamic principles governing natural flyers, engineered systems can be designed to efficiently harness these innate phenomena using simple, lightweight structures.

However, the structural complexity of FWRs presents challenges in implementing active control (Ref.9)(Ref.12). To achieve active control, based on the research conducted in 2021, a 60g prototype along with a ground test platform, and a Simulink-based FWR digital-twin simulator were developed. By periodically adjusting the wing pitch angle, we successfully generated control moments, enabling active control of the FWR MAV configuration. The FWR MAV design, which emulates the intricate motion of insects(Ref.13) involving flapping and rotation, capitalizes on the unsteady aerodynamic effects observed in flapping insects at low Reynolds numbers, allowing for low-frequency flapping while maintaining high lift and efficiency. However, this complexity poses significant challenges in establishing the FWR digital-twin simulator. Small Reynolds numbers and unsteady aerodynamic effects caused by flapping make conventional rotorcraft modelling methods ineffective.

To address the challenge of accurate flight dynamics modelling for the bio-inspired FWR MAV, this paper proposes a methodology to enhance model fidelity leveraging real flight test data. The proposed model refinement methodology and simulation framework aim to capture the complex dynamics of the FWR MAV with higher accuracy. The modified modelling approach developed herein enables real-time aerodynamic prediction of this unique bio-inspired platform in simulation. By leveraging experimental data, the model is calibrated to improve fidelity while retaining computational efficiency for real-time application. This study represents an initial step toward closing the gap between simulated and actual performance for this novel bio-inspired aerial platform.

The paper is structured as below. The paper firstly reviews relevant prior work on flapping wing MAV modelling, secondly details the custom-designed FWR MAV prototype and instrumentation, thirdly formulates the aerodynamic model integrating unsteady effects, fourthly tunes model parameters based on flight test measurements, and finally summarizes key results while discussing future work.

## 2. REVIEW

The FWR presents a novel high-efficiency biomimetic flapping wing MAV. In contrast to traditional flapping wing aircraft that rely solely on wing kinematics for lift generation, this innovative MAV employs multiple aerodynamic mechanisms for enhanced performance. As depicted in Figure 1, conventional flapping wing MAVs(Ref.14) (Figure 1a) use only wing flapping to produce downward thrust perpendicular to the stroke plane, enabling vertical take-off and landing (VTOL) capabilities. The FWR configuration (Figure 1b) diverges from this approach; rather than directly utilizing flapping-induced thrust for VTOL, it first converts the thrust into passive rotor rotation. The considerable lift generated by the rotating wing is then exploited for sustained VTOL flight.

By effectively decoupling the flapping actuation from the primary lift-production through the introduction of a rotational degree of freedom, more design freedom is unlocked. This allows the wing kinematics to be tailored specifically for high-thrust generation, while the rotor geometry is optimized for maximal lift efficiency during climb. This bio-inspired, dual-aerodynamic mechanism paradigm underpins the FWR MAV's exceptional flight performance within a compact, lightweight package.

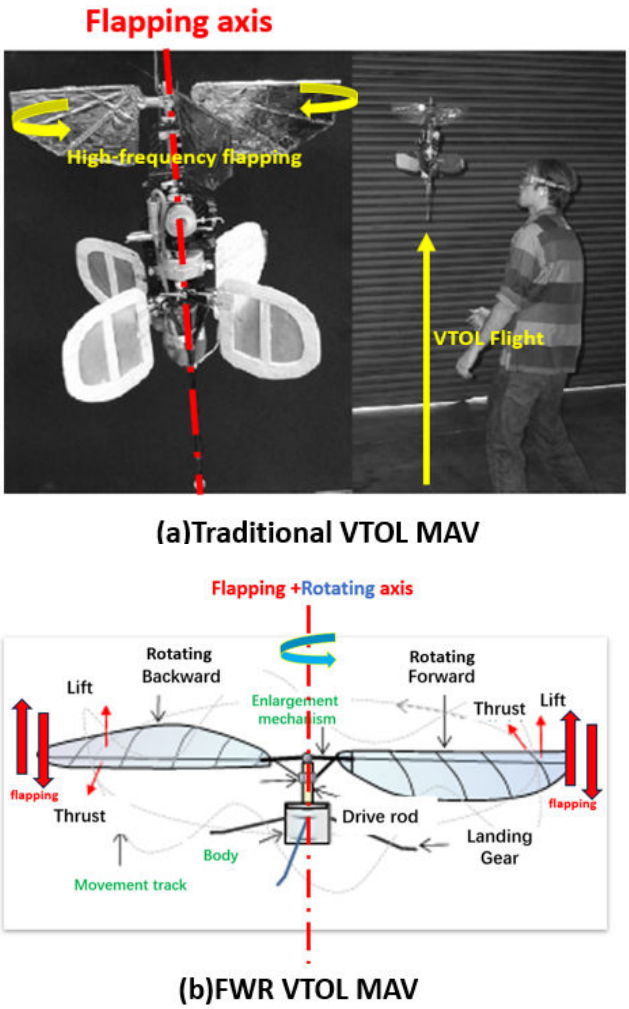


Figure 1 Comparison between Traditional MAV and FWR MAV

Previous research shows that compare with traditional flapping wing which used HF(Horizontal Flapping) and IF(Inclined Flapping)(Ref.6)The FWR lift generation strategy can produce a $C_{l_{max}} = 3.99$ higher than HF $C_{l_{max}} = 1.99$ and IF $C_{l_{max}} = 1.82$ which widely used in traditional flapping wing MAV(Ref.6) (Ref.15– Ref.17).In 2021, a proof-of-concept prototype of the FWR MAV was developed with a 34 cm wingspan. This achieved a maximum take-off weight (MTOW) of 80 g, significantly surpassing the capacity of platforms with similar scale. For example, the renowned DelFly II has a MTOW of just 16.07 g under a 28 cm wingspan. This demonstrates the substantial lift enhancement afforded by the FWR paradigm. However, the current

FWR prototype employs a passive flight mode, while the DelFly incorporates control actuation.

Table 1 Performance comparsion of MAVs with different configurations

| | Configuration | Mass (g) | Wingspan (cm) | Flight Endurance (min) |
|---|---|---|---|---|
| **Cranfield FWR** | **Flapping wing Rotor** | **60** | **25** | **Unknown** |
| DelFly I | Tailed Biplane | 21 | 50 | Unknown |
| DelFly II | Tailless Biplane | 16 | 28 | 15 |
| Delfly Micro | Tailed Monoplane | 3 | 10 | 2 - 3 |
| Delfly Nimble | Tailless Monoplane | 29 | 33 | 5 |
| DARPA-Nano Hummingbird | Tailless Monoplane | 19 | 16 | 11 |
| Ku-Beetle-s | Tailless Monoplane | 15.8 | 10 | 9 |
| Robotic Hummingbird | Tailless Monoplane | 12 | 7 | Unknown |

Table 1 presents a performance comparison between established biomimetic MAV configurations from literature(Ref.2, Ref.5, Ref.11, Ref.18– Ref.24) and the FWR concept for wingspans under 50 cm. The FWR achieves the highest lift capacity, defined as MTOW normalized by wingspan. Its 80 g MTOW corresponds to a lift capacity of 2.4 g/cm, more than double that of other flapping-wing designs.

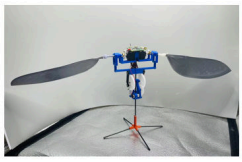
Cranfield FWR

DelFly I

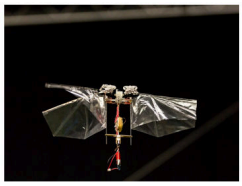
DelFly Nimble


DARPA-Nano Hummingbird

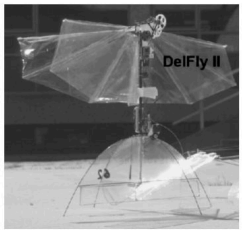

DelFly II


DelFly Micro

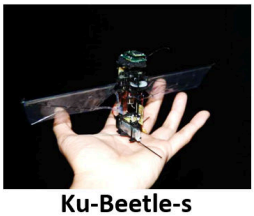
Ku-Beetle-s

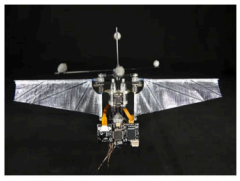
Robotic Hummingbird

Figure 2 Traditional flapping wing configuration

The research conducted in 2021 demonstrated that the FWR MAV with this configuration can carry a larger payload than the traditional pure flapping MAV, thus confirming its promising potential for development. Therefore, our current focus is on addressing its inherent lack of control, aiming to establish a controllable FWR MAV.

As depicted in Figure 1, a distinctive feature of the bio-inspired rotor is its tendency to passively align with the body orientation. This characteristic provides valuable insights for attitude control system design. A further improved FWR variant has been proposed, as shown in Figure 3, incorporating two servos at the flapping wing roots to enable pitch axis control. Additionally, a 300 Hz gyroscope and 500 Hz magnetic heading sensor are integrated into the flight controller to sense real-time rotor azimuth and elevation angles:

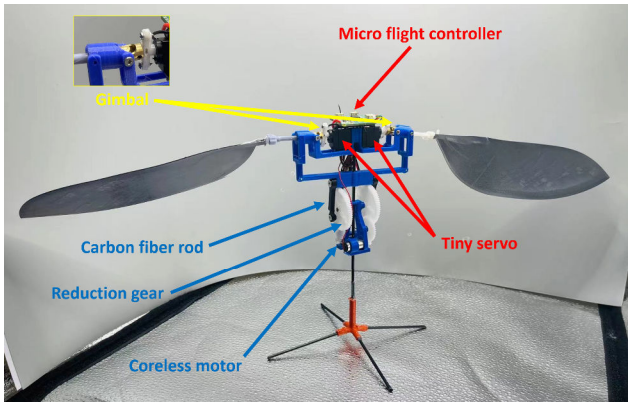


Figure 3 Overall structure of MAV physical model

This enhanced sensorimotor configuration, combined with the innate passive alignment of the rotor, is expected to facilitate precision attitude regulation. The heading sensor provides fast measurement of yaw deviations for correcting undesired rotations. Meanwhile, the gyroscope captures pitch and roll disturbances to maintain stability. At the wing root, two lightweight DM-A0020 servos, each weighing only 2g, are installed to control the pitch axis of the

blade. In the lower part of the aircraft, two brushless motors drive the linkages through a gear reduction system, causing the wings to flap up and down at the desired angles. By adjusting the speed of the brushless motors, the flapping frequency can be controlled, thus, the lift can be adjusted. The control of both the servos and the brushless motors can be programmed through the micro flight controller mounted at the top.

Unlike previous FWR MAV implementations (Ref.12, Ref.17), the present design adopts an integrated rotor head and fuselage structure that rotates as a single rigid unit (Figure 4b), diverging from the decoupled configuration used in prior works (Ref.7, Ref.15, Ref.16) (Figure 4a). This unified rotation scheme significantly reduces modelling complexity compared to a bearing-coupled fuselage and rotor. In the decoupled paradigm, the passive fuselage rotation depends entirely on complex bearing friction forces that are challenging to accurately model and predict. Additionally, the uncontrolled fuselage motion hinders attitude observation by onboard sensors.

In contrast, consolidating the rotor head and fuselage into a single rotating assembly eliminates friction-induced coupling and enables the system to be represented as a solid body. This greatly simplifies mathematical modelling while preserving the innate benefits of passive rotor alignment. The unified rotation also maintains consistent body-fixed sensor alignments, avoiding complications from sensor-airframe misalignments induced by unconstricted fuselage motion.

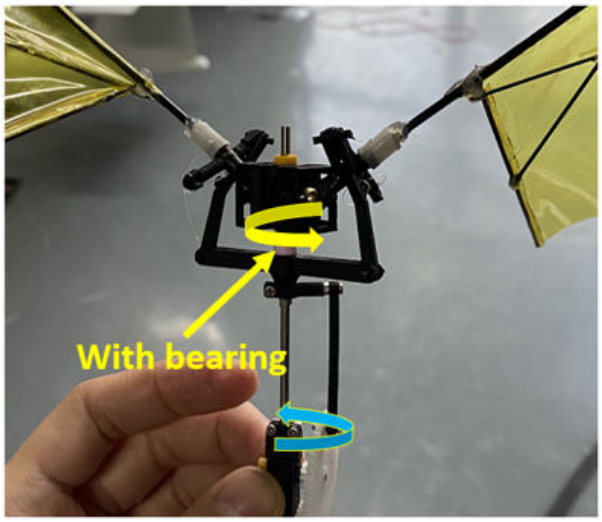


(a)FWR with bearing

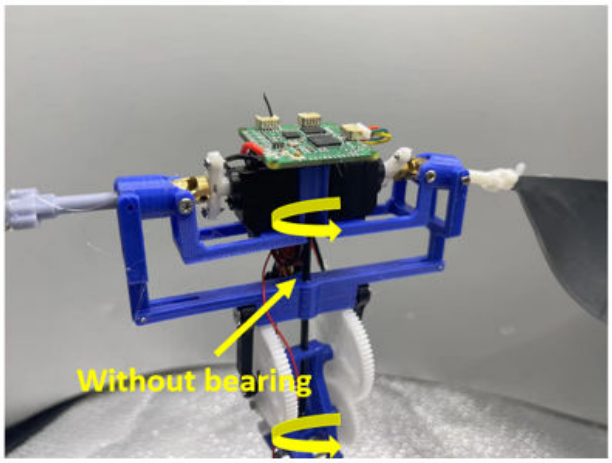


(b)FWR without bearing

Figure 4 The difference between the old FWR (a) and the new FWR design (b)

## 3. EXPERIMENTAL PLATFORM

To enable systematic experimentation and data collection, a ground test platform has been developed with full independent control authority over the FWR MAV wing kinematics. As depicted in Figure 5, this customized test stand provides precise actuation and measurement of the key flapping wing motion variables - flapping angle, pitch angle, and flapping plane angle.:

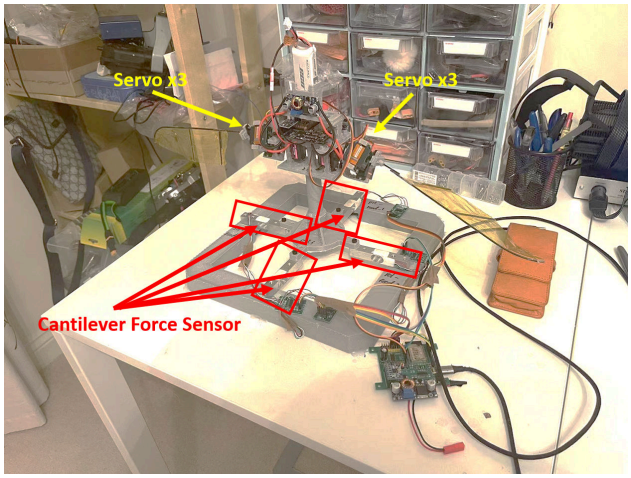


Figure 5 FWR MAV test platform

The test apparatus, shown in Figure 5, utilizes three servo motors to independently control each wing's pitch, flapping, and flapping plane angles. The entire rig is capable of rotation. Four force sensors are positioned beneath the platform to measure the complete force vector generated by the FWR MAV. Post-processing derives the lift and torque values from the measurements.

This integrated test stand enables thorough characterization and validation of the bio-inspired MAV's manoeuvring abilities and performance in a controlled setting prior to free flight trials. It provides an effective digital twin test bench for researchers to fine-tune and optimize control algorithms and mechanical designs, facilitating enhanced flight capabilities.

The focus of this work is to leverage the ground test platform to establish accurate dynamic and kinematic models that can predict the FWR's lift and moment generation. By correlating the measured forces and motions from the rig, the model can be calibrated to capture the underlying physics governing the complex flapping rotor aerodynamics. The validated simulation tools will then support the future development of this novel MAV platform through virtual design iterations and prototyping before resource-intensive fabrication and testing.

## 4. MODELING OF NEW FWR CONFIGURATION

### 4.1. FWR coordinate system definition

For the FWR MAV, the coordinate systems for the modelling are depicted in Figure 6.

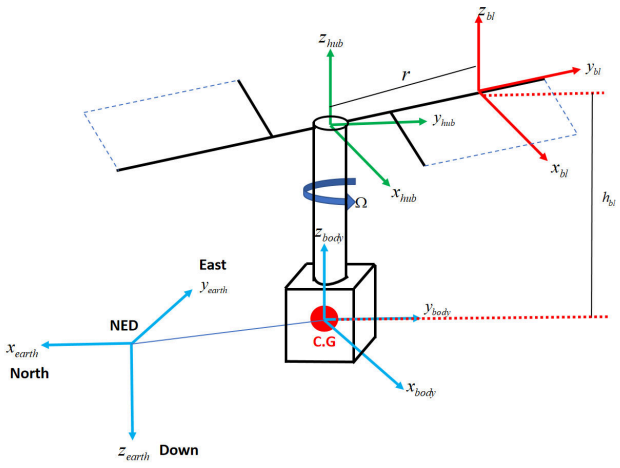


Figure 6 Coordinate system of FWR MAV

Among them, $xyz_{earth}$ is the ground coordinate system, $xyz_{body}$, and $xyz_{hub}$ are the body coordinate system and the rotor hub coordinate system, respectively. $xyz_{bl}$ represents the blade element coordinate system of the rotor. In this design, since the rotor and the body are fixed and rotate together at the same angular velocity $\Omega$, these two coordinate systems are equivalent to being fixed at both ends of a rigid body, with a vertical offset $h_{bl}$ between them.

### 4.2. Modelling velocity at blade elements

Let the incoming flow velocity in the *x*, *y*, and *z* directions of the blade element coordinate system be $W_x$, $W_y$, and $W_z$ respectively. Set the relative flow velocity of the hub coordinate system as $V_{\infty hub}$, decompose it along the *x*, *y*, and *z* directions of the hub coordinate system, and three velocities can be decomposed: $V_{\infty hub\_x}$, $V_{\infty hub\_y}$, $V_{\infty hub\_z}$ .If only consider $V_{\infty hub\_x}$ and $V_{\infty hub\_z}$, there are(Ref.25):

(1) $$W_x = -\Omega r\cos\beta - V_{\infty hub\_x}\sin\Psi$$

(2) $$W_y = V_{\infty hub\_x}\cos\Psi\cos\beta - (v_i - V_{\infty hub\_z})\sin\beta$$

(3) $$W_z = (v_i - V_{\infty hub\_z})\cos\beta + v_\beta + V_{\infty hub\_x}\cos\Psi\sin\beta$$

Among them, $v_\beta$ is the flapping velocity, $v_\beta = -\frac{d\beta}{dt}r.(v_i - V_{\infty hub\_z})\,cos\,\beta$ is the rotor-induced velocity coupled with the component of the incoming flow in the z-axis direction of the hub coordinate system.

$V_{\infty hub\_x}\,cos\,\Psi\,sin\,\beta$ is the component of the incoming flow in the x direction of the hub coordinate system on the $z_{blade}$ coordinate axis. $r$ is the position of blade element in the span direction from the root,$V_{\infty hub\_x}$ is the income flow along the x-axis of the hub coordinate system,$\psi$ is the rotor azimuth angle, $\beta$ is the flapping angle.

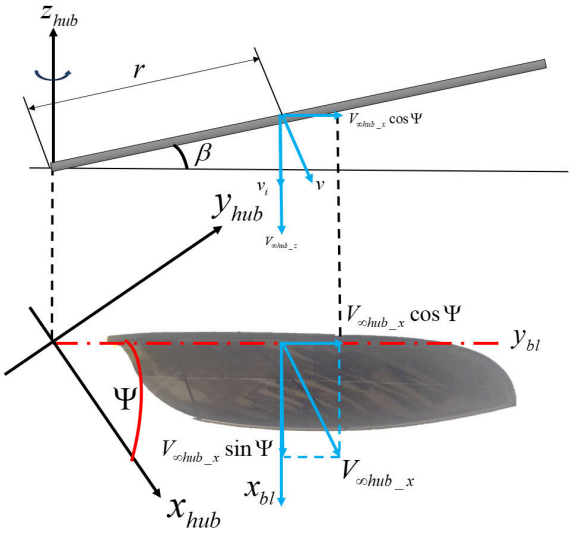

Figure 7 Velocity definition at hub coordinate system

To analyse the blade element of the flapping wing, the AoA (angle of attack) and the velocity of the blade element are defined in Figure 8.

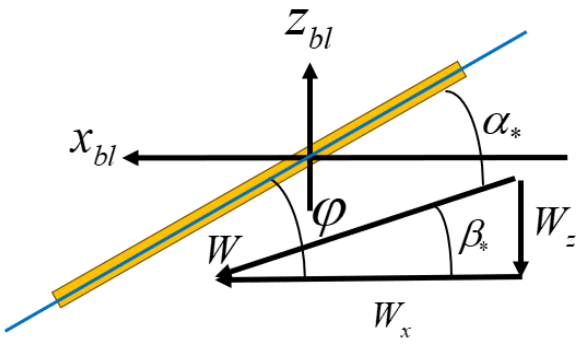


Figure 8 angles defined in the blade element

(4) $$\beta_* = \arctan\frac{W_z}{W_x}$$

(5) $$a_* = \varphi - \beta_*$$

in which, $\varphi$ is the pitch angle of flapping wing. $a_*$ is the effective AoA. It is obtained by the difference between the pitch angle and the angle of the incoming flow velocity $\beta_*$ . The latter is derived from the arc tangent on the Z-direction velocity and the X-direction velocity obtained from equation(Eq. (1), Eq. (3)).

### 4.3. Biomimetic flapping angle $\beta$ and pitching angle $\varphi$

Calculating the wing velocity requires knowledge of the pitching angle $\varphi$ and flapping plane angle $\beta$. Unlike helicopters which actively control $\varphi$ via a swashplate and use passive methods for β(Ref.25), both angles are actively controlled in the FWR MAV. Two servos independently modulate φ on each wing by driving a linkage to enact flapping. This enables efficiency optimization by tuning $\varphi$ and $\beta$, which represent key parameters governing differences in insect flight performance. By decoupling and independently actuating $\varphi$ and $\beta$, the FWR paradigm permits adjusting these angles for different flight phases. High thrust modes can exploit more aggressive, high-amplitude flapping with steeper $\beta$ for vertical lift. Cruise phases can adopt flatter $\beta$ and lower $\varphi$ for efficiency. Mimicking the wing kinematics of high-performing natural flyers is also possible.

This dual-angle control differentiates the FWR from helicopters and even most flapping wing MAVs. It facilitates harnessing unsteady phenomena for performance exceeding traditional designs restricted to passive stroke plane variation(Ref.15). However, modeling the wing dynamics and loads with two controlled degrees of freedom poses challenges compared to single DOF platforms. This complexity motivated the current work to formulate an enhanced model capturing the aeromechanic couplings.

In order to obtain high lift efficiency, Cranfield's team compared a variety of φ and β combination modes in previous studies, including fruit flies, hummingbirds and dragonflies. Finally, the φ and β combination mode of dragonflies proved to have the highest efficiency. Its average lift coefficient can reach $\bar{C}_l = 1.93$, (Ref.26) which is much higher than that of other insects.

Unlike the symmetrical flapping kinematics utilized by most insects (Figure 9a), dragonflies employ an asymmetric half-stroke strategy as depicted in Figure 9b(Ref.13). During the upstroke, the pitching angle φ is maintained at approximately 90° to minimize drag. Meanwhile, on the downstroke φ becomes near 0°, generating substantial lift. This distinct flapping pattern allows dragonflies to achieve markedly higher flight efficiency compared to other insects.

By primarily producing thrust on just the downstroke while minimizing exertions during upstroke, the half-stroke mode reduces wasted energy and harnesses aerodynamic mechanisms like delayed stall for additional lift augmentation. The capability of the FWR MAV to actively control both stroke plane and pitch enables replicating these efficient biologically-evolved flapping profiles. Implementing asymmetric kinematics based on dragonflies(Ref.13) or other natural flyers with verified performance represents a promising route for optimization.

However, modelling the associated unsteady aerodynamics and complex wake interactions introduces additional challenges versus symmetric flapping(Ref.27). The current work aims to expand modelling fidelity to capture these nuances.

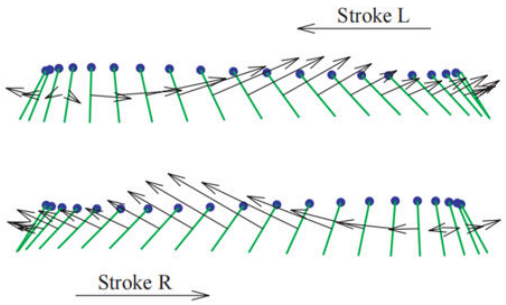


**(a) Symmetrical flapping**
**Traditional flapping insects**

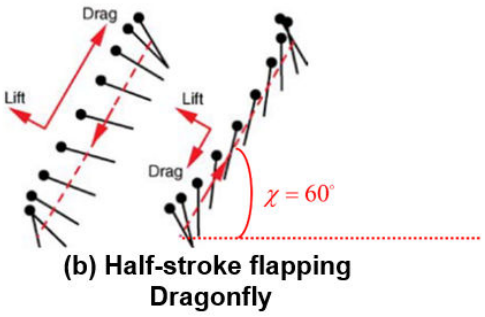


Figure 9 The difference between traditional flapping wings (Ref.28)(a) and dragonfly flapping wings (b)

Therefore, the study of these bionic results led us to adopt the dragonfly-like flapping mode in FWR. However, our FWR cannot completely imitate the multi-degree-of-freedom flapping curve of a dragonfly. For instance, in real dragonfly, its flapping plane will be at an angle $\chi = 60^{\circ}$, as depicted in Figure 9b above. The dragonfly can actively control the angle of the flapping plane by adjusting this $\chi$ angle, enabling the wings to move back and forth in the horizontal plane and generate incoming flow velocity(Ref.13), thereby increasing the lift. Moreover, by adjusting this angle, the dragonfly can achieve control over the direction of the force vector, facilitating the transition from hovering to forward flight. This dynamic control of the flapping angle is a crucial adaptation that enables the dragonfly to exhibit remarkable manoeuvrability and versatility in its flight behaviour.

The reason why we can't completely imitate the multi-degree-of-freedom flapping curve of a dragonfly is mainly due to the trade-off between control complexity and weight considerations. To achieve $\chi$ angle controllability like a dragonfly's wing, two additional DM-A0020 servos (weighing 2g each) are required. However, adding servos would lead to a sacrifice nearly 26%(4g) of the load capacity under MTOW (Maximum Take-off Weight) conditions.

In contrast, the attitude control of the FWR MAV can be achieved directly by adjusting wing pitch angle $\varphi$ via cycle control, like a helicopter, without the need to change the angle $\chi$ of the flapping plane. As a result, the degree of freedom of the flapping plane of the dragonfly wing is removed in our FWR MAV. During the actual FWR MAV's imitation of the dynamic movement of dragonfly flapping, the flapping plane angle $\chi$ set as a constant value of 90 degrees. This constitutes the main difference between the flapping curve of the FWR MAV and the real dragonfly.

The pitch angle formula used by the FWR MAV can be represented as follows(Ref.29):

if $t$ belong $(-\frac{\Delta T}{2}, \frac{\Delta T}{2})$, and then:

$$\varphi(t) = \frac{\varphi_u + \varphi_d}{2} + \frac{\varphi_d + \varphi_u}{2}\sin(\pi \frac{t}{\Delta T}) \tag{6}$$

if $t$ belong $(\frac{\Delta T}{2}, \frac{T-\Delta T}{2})$, and then:

$$\varphi(t) = \varphi_d \tag{7}$$

if $t$ belong $(\frac{T-\Delta T}{2}, \frac{T+\Delta T}{2})$, and then:

$$\varphi(t) = \frac{\varphi_u + \varphi_d}{2} + \frac{\varphi_d + \varphi_u}{2}\sin(\pi \frac{T/2 - t}{\Delta T}) \tag{8}$$

if $t$ belong $(\frac{T+\Delta T}{2}, T - \frac{\Delta T}{2})$, and then:

$$\varphi(t) = \varphi_u \tag{9}$$

According to literature (Ref.29). Dimensionless wing pitch times of dragonflies is $\Delta T = 0.4$. Meanwhile it's maximum pitch angle $\varphi_u = 170^{\circ}$ , and minimum pitch angle $\varphi_d = 65^{\circ}$ .

The flapping angle $\beta$ obeys the following formula:

$$\beta = \beta_{INIT} + \frac{\beta_{AMP}}{2}\cos(2\pi ft) \tag{10}$$

$\beta_{INIT}$ is the initial flapping angle, which is set to 30°. $\beta_{AMP}$is the flapping amplitude, limited by the structure shown in Figure 3, the flapping amplitude is limited to 60°, $f$ is the flapping frequency in Hz, and $t$ is the time of the current flapping cycle.

The experimental results indicate that when the flapping plane angle $\beta$ is set to 0° while maintaining the maximum pitch angle $\varphi_u = 170^{\circ}$, it results in a high AoA during flapping. The AoA introduces considerable drag, diminishing the rotor's passive angular velocity and subsequently decreasing the lift produced by the rotor's rotation. Given the constraints of the mechanical structure, the flapping angle of the FWR MAV ($\beta_{INIT}$ =0, $\beta_{AMP}$ =70°) exhibits a subtle variation compared to that of a dragonfly ($\beta_{INIT}$=15°, $\beta_{AMP}$=60°). The adjustment in the flapping angle has been tested and confirmed to enhance the lift during

the FWR MAV's flight, while adhering to the constraints of its mechanical design.

The flapping and pitching angle parameters of FWR MAV have been defined in Table 2:

Table 2 FWR MAV angle parameters

| FWR MAV angle parameters | |
|---|---|
| $\beta_{INIT}$ | 0° |
| $\beta_{AMP}$ | 70° |
| $\varphi_u$ | 90° |
| $\varphi_d$ | 50° |

### 4.4. Force of blade elements and unsteady aerodynamics correction

To minimize inertial forces induced by flapping, the FWR MAV wing surface is constructed from polyimide film with a thickness of just 0.015 mm and density of 1.4 g/cm$^3$. Assuming negligible elastic twist, the wing can be modeled as a flat plate airfoil. The blade element coordinates are defined in Figure 10.

The ultra-lightweight polyimide provides adequate stiffness while reducing flapping power requirements. Treating the wing as a flat plate is a common assumption in flapping wing aerodynamic models and avoids uncertainties in airfoil data at low Reynolds numbers. However, this approximation neglects wing curvature effects on bound circulation and stall behaviour. Future refinements could incorporate experimental data mapping lift curve characteristics across Reynolds numbers ranging from $10^2$ to $10^4$.

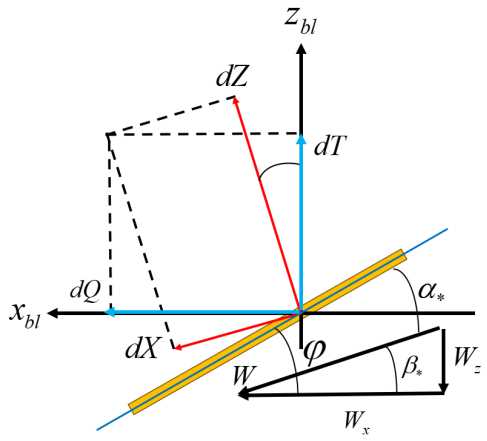


Figure 10 Coordinates definition of FWR blade elements

Nevertheless, the flat plate assumption serves as a useful starting point for formulating the initial model. The goal is to isolate the fundamental unsteady mechanisms before introducing additional complexity. Once validated against benchtop experiments, progressively transitioning to higher-fidelity airfoil representations based on ground flight testing data represents a logical model maturation path for capturing real-world FWR dynamics with minimal empirical approximations.

In Figure 10,$dZ$ is perpendicular to the direction of the incoming flow, and $dX$ aligns with the direction of the incoming flow. Furthermore, the forces $dT$ and $dQ$ acting on the $x_{bl} - z_{bl}$ coordinate system can be calculated as follows:

$$dT = dZ\cos\beta_* - dX\sin\beta_* \tag{11}$$

$$dQ = dX\cos\beta_* + dZ\sin\beta_* \tag{12}$$

Among them, $dX$ and $dZ$ can be obtained by the following equation:

$$W = \sqrt{(W_x)^2 + (W_z)^2} \tag{13}$$

$$dZ = \frac{1}{2}C_y(\alpha_*)\rho W^2 c(r)dr \tag{14}$$

$$dX = \frac{1}{2}C_z(\alpha_*)\rho W^2 c(r)dr \tag{15}$$

The dX and dZ forces derived previously represent translational terms. However, under the low Reynolds number, and unsteady conditions inherent to FWR flight, accurately modelling the wing aerodynamics requires considering additional phenomena. This motivates adopting a quasi-steady modelling approach, incorporating forces beyond just translation. Specifically, a quasi-steady model includes added mass forces and rotational forces in addition to the translational profile drag and lift elements. The added mass force accounts for the reaction arising from the flapping wing accelerating the surrounding air.

Rotational forces (Ref.30) model the circulation generation and shedding processes that produce lift. These unsteady phenomena deviate significantly from static airfoil theory. By incorporating them, the quasi-steady model aims to provide greater physical fidelity compared to a strictly translational representation. However, modelling rotational aerodynamics introduces empirical approximations of lift behaviour. An incremental modelling approach can help isolate and quantify these uncertainties:

(16) $$dF_A(r,t) = \frac{\pi}{4}\rho c(r)^2 a_n dr$$

Among them， $\rho$ is the air density, $c(r)$ is the chord length in location *r*, $a_n$is the acceleration of reference point which represents the mass of this blade element. $dr$ is the width of the blade elements, and the $\frac{\pi}{4}\rho c(r)^2$ is the mass of the air which has been accelerated by flapping. $a_n$ can be calculated using the flowing equation:

(17) $$a_n = r\ddot{\beta}\sin\varphi + c(r)\dot{\beta}\cos\varphi\sin\varphi + c(r)\ddot{\varphi}$$

Where:

$\ddot{\beta}$: Angular acceleration of the flapping angle

$\dot{\beta}$: Angular rate of the flapping angle

Finally, the added mass forces on $x_{bl}$ axis and $z_{bl}$ axis can be given by the following equation:

(18) $$\begin{cases} dF_{A\_x\_bl} = -\frac{\pi}{4}\rho c(r)^2 a_n \sin\varphi dr \\ dF_{A\_z\_bl} = \frac{\pi}{4}\rho c(r)^2 a_n \cos\varphi dr \end{cases}$$

Beyond the influence of the added mass force, the change in the angle signifies the pitch axis rotation of the blade elements. This rotation induces an airflow reaction force, termed the “Rotation force“(Ref.30). The formula for this force is as follows:

(19) $$dF_{rot} = c_{rot}\rho V_\beta \dot{\varphi} c^2(r) dr$$

According to the literature (Ref.6), $c_{rot}$is selected as 0.05, and further, we can get the Rotation Force of the two axes:

(20) $$\begin{cases} dF_{rot\_x\_bl} = -dF_{rot}\sin\varphi \\ dF_{rot\_z\_bl} = dF_{rot}\cos\varphi \end{cases}$$

Finally, $dZ$ , $dX$ equations are corrected by added mass force and Rotation force, as follows:

(21) $$dZ = \frac{1}{2}C_z(\alpha_*)\rho W^2 c(r)dr + dF_{A\_z\_bl} + dF_{rot\_z\_bl}$$

(22) $$dX = \frac{1}{2}C_x(\alpha_*)\rho W^2 c(r)dr + dF_{A\_x\_bl} + dF_{rot\_x\_bl}$$

### 4.5. 6 DOF rigid body mechanical model

After calculation of $dX$ and $dZ$, The subsequent step involves deriving the 6DOF rigid body mechanical model for the FWR. This will enable us to formulate the dynamic and kinematic equations that characterize the motion of the FWR MAV in real-world scenarios. First, the $dT$and $dQ$ obtained earlier has decomposed into the hub coordinate system, resulting in the following formula.

The component of *dT* in the hub coordinate system:

(23) $$dT_h = dT\cos\beta$$

Backward force in hub coordinate system:

(24) $$dH_h = dQ\sin\psi - dT\sin\beta\cos\psi$$

Lateral force in hub coordinate system:

(25) $$dS_h = -dQ\cos\psi - dT\sin\beta\sin\psi$$

Torque in hub coordinate system:

(26) $$dM_{kh} = dQr\cos\beta$$

By integrating, the total thrust of the propeller disc can be obtained:

(27) $$T = k\frac{1}{2\pi}\int_0^{2\pi}\int_{r0}^{r1}\frac{dT_r}{dr}drd\Psi$$

Based on the coordinate system relationship shown in Figure 7, $dH_h$,$dT_h$, $dS_h$,$dM_{kh}$in the hub coordinate system can be transform into the body coordinate system. This transformation allows us to obtain the three-axis force formula and three-axis torque formula for the FWR MAV:

(28) $$\begin{cases} {}^{body}F_x = \sum_{i=1}^{n} dH_h \\ {}^{body}F_y = \sum_{i=1}^{n} dS_h \\ {}^{body}F_z = -mg + \sum_{i=1}^{n} dT_h \end{cases}$$

(29) $$\begin{cases} {}^{body}M_x = \sum_{i=1}^{n} r(\cos\beta)dT_h - h_{bl}dS_h \\ {}^{body}M_y = \sum_{i=1}^{n} h_{bl}dH_h \\ {}^{body}M_z = \sum_{i=1}^{n} r(\cos\beta)dH_h \end{cases}$$

According to Newton Euler's formula, the angular velocity equation is：

$$(30) \qquad {}^{body}\dot{\omega} = I^{-1}({}^{body}M - {}^{body}\omega \times (I \cdot {}^{body}\omega))$$

FWR acceleration equation:

$$(31) \qquad \begin{cases} {}^{body}a_x = \dfrac{{}^{body}F_x}{m} \\ {}^{body}a_y = \dfrac{{}^{body}F_y}{m} \\ {}^{body}a_z = \dfrac{{}^{body}F_z}{m} \end{cases}$$

Furthermore, we will transform the force and moment from the body coordinate system to the earth coordinate system, adopting the Yaw-Pitch-Roll sequence for rotation :

Then the total transformation matrix is:

$$(32) \qquad R(\psi,\theta,\phi) = R_z(\psi)R_y(\theta)R_x(\phi)$$

Ultimately, we derive the expression for the FWR MAV's acceleration in relation to the Earth coordinate system:

$$(33) \qquad \begin{bmatrix} {}^{earth}a_z \\ {}^{earth}a_y \\ {}^{earth}a_x \end{bmatrix} = R(\psi,\theta,\phi) \begin{bmatrix} {}^{body}a_z \\ {}^{body}a_y \\ {}^{body}a_x \end{bmatrix}$$

## 5. MODEL FIDELITY IMPROVEMENT THROUGH TUNING

### 5.1. Model structure improvement through new forms of aerodynamic coefficients

$C_x$ is the lateral force coefficient used to calculate $dX$by using Eq. (19). $C_z$ is the lift coefficient used to calculate $dZ$ by using Eq. (18).

The values in question have been demonstrated to profoundly influence the lift and thrust calculations of flapping wing systems. However, the FWR MAV amalgamates the unsteady aerodynamic traits of a flapping wing with the steady aerodynamic properties of rotorcraft. Additionally, its compact wing size results in a low Reynolds number. Consequently, its $C_x$ and $C_z$ values necessitate meticulous consideration and fine-tuning(Ref.31– Ref.33).

Due to the application of the dragonfly's flapping curve in FWR MAV, the pitch angle φ of the wings can be maximum to 90°. Therefore, the correction of unsteady aerodynamic forces at low Reynolds number and high angle of attack must be introduced in modelling.

Kirchhoff, Helmholtz, and Rayleigh (Ref.13) have studied the Lift coefficient and Drag coefficient in high AoA case. They got the $C_x$, $C_z$ coefficient for the AoA ranging from 0 ° to 90 °. In our FWR study, this theory has been extended from AoA -90 ° to 90 °, as follows:

$$(34) \begin{cases} C_z = \pi \sin 2\alpha / (4 + \pi \sin\alpha) & \alpha \in (0,90] \\ C_z = -\pi \sin(-2\alpha) / \left[4 + \pi \sin(-\alpha)\right] & \alpha \in [-90,0] \end{cases}$$

$$(35) \begin{cases} C_x = \pi \sin^2 \alpha / (4 + \pi \sin\alpha) & \alpha \in (0,90] \\ C_x = -\pi \sin^2(-\alpha) / \left[4 + \pi \sin(-\alpha)\right] & \alpha \in [-90,0] \end{cases}$$

However, the above formula does not actually consider the correction of Reynolds number $Re$, but only applies to the case of steady flow at regular Reynolds number.

The Reynolds number under our FWR application can be calculated with the following formula:

$$(36) \qquad \mathrm{Re} = \frac{\overline{c}U_{ref}}{v}$$

$v$ is fluid viscosity and $U_{ref}$ is the reference velocity. $U_{ref} = fl$, and $l$ is the distance travelled by a point per flapping cycle. H Li, S.Guo has calculated the Reynolds number of FWR MAV: Re~3500, which is very small. Therefore, the influence of Reynolds number on $C_z$ and $C_x$ coefficients must be considered. Researchers such as H Li, S. Guo have considered this effect. They have adopted the work of (Ref.6) in their research on FWR, modified the Lift coefficient by $Re$, and obtained the following formula:

$$(37) \qquad \begin{cases} C_z = C_{z\max} \sin(2a_*) \\ C_x = \left(\dfrac{C_{x\max} + C_{x0}}{2}\right) - \left(\dfrac{C_{x\max} - C_{x0}}{2}\right)\cos(2a_*) \end{cases}$$

According to the CFD results (Ref.6), H Li, S. Guo calculated that $C_{xmax} = 3.24$ and $C_{zmax} = 1.7$. These two parameters align the Quasi-Steady model with experimental results observed at 10Hz.

The FWR MAV developed in this work controls lift via flapping frequency modulation over a wide 0-20Hz range, achieving 0-60g lift authority. Therefore, the mathematical model must provide accurate predictions across varied flapping rates. To validate performance, extensive flapping wing lift experiments

were conducted on the test stand across 6-18Hz. Predictions using two modelling approaches were compared to measurements:

1. Method 1 - Quasi-steady model using Kirchhoff, Helmholtz and Rayleigh principles.

2. Method 2 - Quasi-steady model with Reynolds number corrections (H Li, S. Guo).

Figure 11a and 11b present the results. The root-mean-square error (RMSE) quantified prediction accuracy.

The need for broadband frequency-domain fidelity stems from implementing variable flapping for manoeuvring and control. By correlating simulations and experiments across operating points, modelling deficiencies at specific conditions can be identified. This enables systematic refinement to improve predictive range. If certain effects (e.g. rotational lift) only become prominent at higher frequencies, incremental modelling can isolate these. This integrated approach combining experimentation, simulation, and iterative model tuning provides a pathway for maturing the physics-based aerodynamic representation across the flight envelope.

The RMSE value is defined as follows:

$$RSME = \sqrt{\frac{\sum (y_i - \hat{y}_i)^2}{n}} \tag{38}$$

The smaller the RSME, the smaller the prediction error, and vice versa, it means the greater the prediction error.

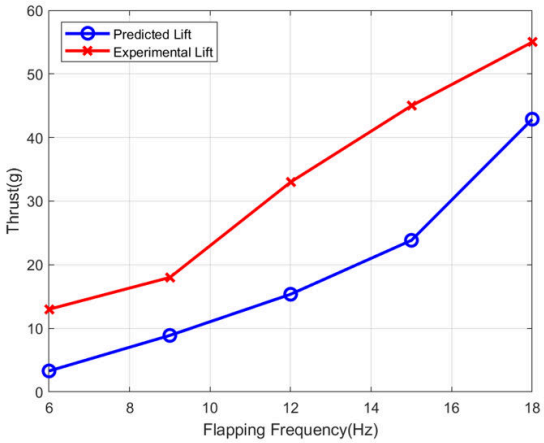


**(a) Helmholtz and Rayleigh (Method 1)**

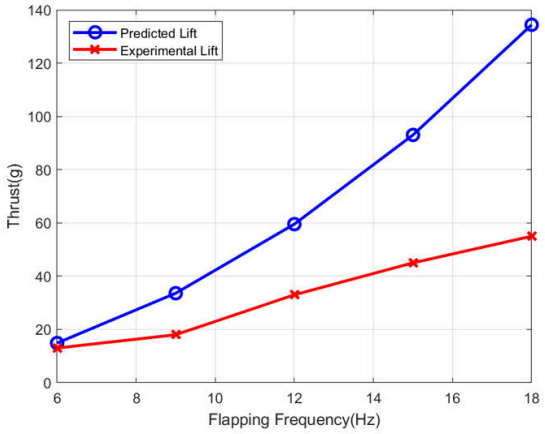


**(b) H.Li and S.Guo (Method 2)**

Figure 11 Comparison of experimental lift & BET predicted lift(Method 1&2)

Method 1 (as depicted in Figure 11a) does not account for the influence of the Reynolds number. It solely contemplates variations within a high angle of attack and typical Reynolds number range. As a result, the quasi-steady lift prediction is underestimated, with the predicted lift ranging between 25% and 78% of the experimental lift, yielding an RMSE of 14.72. The majority of the lift predicted by the Method 1 model is attributed to the steady aerodynamic effect, suggesting a potential overfitting to the lift generated by this steady influence.

Method 2 (illustrated in Figure 11b) incorporates the effects of low Reynolds numbers and employs empirical corrections to $C_{xmax}$ and $C_{x0}$ based on CFD simulation results at 10Hz low-frequency flapping. While these adjustments enhance accuracy at lower frequencies, the model encounters challenges in predicting lift at higher frequencies. The predicted lift substantially exceeds the experimental values, ranging between 114% and 244%. With RMSE of 43.73, there's a notable divergence between the predicted and observed values. Particularly towards the curve's latter segment, the predicted lift is nearly double the experimental outcome, indicating a significant overestimation. This disparity underscores potential limitations in the predictive model, necessitating further refinements to bolster its precision and reliability.

This overestimation suggests limitations in modelling the transition from unsteady flapping-dominated flows at low frequencies to increased rotational influence at

higher rates. The assumed overfitted unsteady corrections likely break down as rotational forces become prominent. Addressing this overfitting issue is crucial for accurate FWR lift prediction over 0-20Hz.

The FWR combines flapping and rotating lift components. Experimental observations and simulation results imply primarily unsteady flapping forces at low speeds, transitioning to steady rotational dominance at high speeds. Method 2 overfits the model to the unsteady low-speed regime, losing fidelity at rotating-critical high frequencies. A refined approach must capture this dynamic shift in balance between flapping and rotational lift contributions.

Incrementally introducing rotational terms and weighting their influence as a function of flapping rate and geometry could address overfitting. This blended dynamic stall/attached flow model may avoid over-amplifying unsteady corrections across the spectrum. Systematically tuning the model based on force measurements across frequencies can empirically determine appropriate weights and transitions. This semi-empirical approach combining simulations and experiments shows promise for robust FWR lift prediction over diverse aerodynamic regimes.

To achieve a more accurate model, we can use the rotational speed as a reference. For low rotational speeds, more $C_x$ and $C_z$ values calculated by Method 2 can be utilized, whereas for high rotational speeds, more $C_x$and $C_z$ values calculated by Method 1 can be employed. This approach allows for better repair and calibration of the model.

To achieve this goal, a selection model between the results of method 1 and method 2 is implemented as follows:

$$\begin{cases} C_z = \eta C_{z\_method2} + (1-\eta) C_{z\_method1} \\ C_x = \eta C_{x\_method2} + (1-\eta) C_{x\_method1} \end{cases} \tag{39}$$

The selection coefficient $\eta$ plays a critical role in this selection model, as it determines the balance between the contributions of Method 1 and Method 2 based on the current rotor angular velocity. When the rotational angular velocity is larger, a smaller value of $\eta$ would assign a larger proportion to the lift calculated by Method 1. On the other hand, when the rotational angular velocity is smaller, a larger value $\eta$ would give greater significance to the lift calculated by Method 2.

Choosing the appropriate value for the coefficient $\eta$ is of utmost importance, as it directly influences the accuracy of the model's predictions. The optimal value of $\eta$ should be determined through careful calibration and validation using experimental data.

### 5.2. Fidelity Improvement through Tunning Key Parameters

The value of $\eta$ holds significance beyond its impact on the accuracy of our model estimation; it also determines the proportion of unsteady aerodynamic forces and steady aerodynamic forces on the total force acting on the FWR MAV. Understanding this relationship allows for further investigation into how unsteady aerodynamic forces influence the behaviour of the FWR MAV.

The $\eta$ value can be calculated using experimental data. We always got the original experiments data like the flowing Table 3:

Table 3 Experiments data of FWR MAV

| Hz | 6 | 9 | 12 | 15 | 18 |
|---|---|---|---|---|---|
| Motor Voltage(v) | 1.6 | 2 | 2.6 | 3.1 | 3.7 |
| Rotation Speed (RPS) | 3.31 | 5.18 | 7.01 | 9.07 | 11.23 |
| Experimental lift(g) | 13 | 18 | 33 | 45 | 55 |

According to our empirical data, when Ω become high, the unsteady aerodynamics phenomenon will be decreased. So, we can use Ω as input to build the $\Omega - \eta$ equation. Assume there is no incoming flow along axis hub coordinates axis $x$,we can use the experiments data to reverse derivation the value $\eta$ by equation(Eq.(1)-Eq.(27)), after reverse derivation we can get the flowing chart, which indicate the relationship between $\Omega$ and $\eta$:

Table 4 Relationship between Rotation Speed $\Omega$ and $\eta$

| Hz | 6 | 9 | 12 | 15 | 18 |
|---|---|---|---|---|---|
| Motor Voltage(v) | 1.6 | 2 | 2.6 | 3.1 | 3.7 |
| Rotation Speed (RPS) | 3.31 | 5.18 | 7.01 | 9.07 | 11.23 |
| Experimental lift(g) | 13 | 18 | 33 | 45 | 55 |
| $\eta$ value | 0.77 | 0.34 | 0.338 | 0.258 | 0.25 |

Utilizing various filtering methods, we identified the optimal equation to describe these relationships. In this research, we tested the Polynomial filtering, Power filtering, and Rotational filtering methods. Upon comparing the R-square values, the rotational

filtering method (with a numerator degree of 1 and a denominator degree of either 1 or 2) yielded the highest R-square value of 0.937, as depicted in Figure 12.

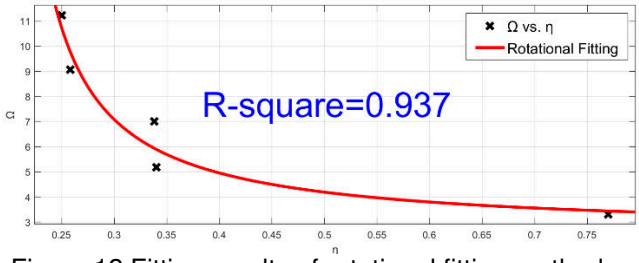


Figure 12 Fitting results of rotational fitting methods

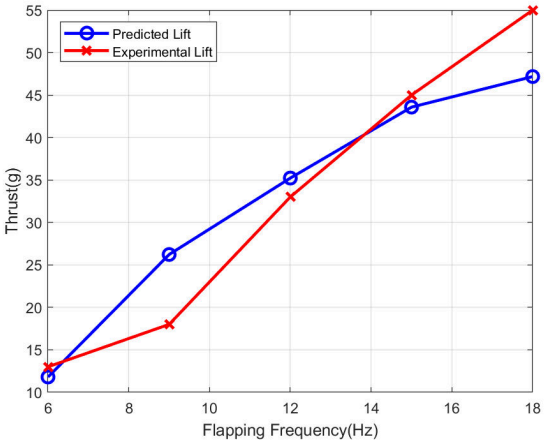


Figure 13 Comparison of experimental lift & BET predicted lift(New Method)

To simplify the $\Omega - \eta$ equation. The flittering result of rotational fitting method has been chosen to use in this research, which indicates the relationship between $\Omega$ and $\eta$:

$$\eta = \frac{p_1\Omega + p_2}{\Omega + q_1} \tag{40}$$

Where,

$$\begin{aligned} p_1 &= 2.578 \\ p_2 &= 0.01922 \\ q_1 &= -0.1881 \end{aligned}$$

Figure 13 illustrates the novel approach to predicting the lift produced by the FWR, juxtaposing it with experimental data spanning a flapping frequency range of 0-20Hz. Relative to the experimental data, the new method yields an RMSE of 5.22. When contrasted with the original, Method 1, and Method 2, the precision of this new approach has seen significant enhancement. It essentially aligns with the actual lift dynamics, especially as the flapping frequency varies extensively between 0-20Hz.

## 6. Flapping Wing Rotor Control

In the previous chapters, we have developed the mathematical model of the FWR MAV. It is evident that, similar to a helicopter, the primary variables influencing the lift of the blade are the pitching angle $\varphi$ of the wing and the flapping angle $\beta$, along with the rotation speed $\Omega$ .In the FWR, the rotation speed $\Omega$ is driven by the thrust $dQ$ generated by the flapping wing flapping, resulting in passive rotation. Therefore, the lift of the blade element is influenced only by the pitching angle $\varphi$ and the flapping angle $\beta$ of the wing.

In the FWR, due to mechanical structural limitations, the amplitude $\beta_{AMP}$ of the flapping angle for both wings cannot be independently adjusted, only the frequency can be altered, and this adjustment synchronously affects both wings. Hence, adjusting $\beta$ it is not a suitable choice for attitude adjustment. However, the pitching angle $\varphi$ of the blades, which can be controlled by two servos, suitable to serves as the means for generating attitude control forces.

Due to the structural similarity between the FWR and the helicopter, the FWR can adjust its attitude similar to the cyclic pitch change of a helicopter. This adjustment is achieved through the use of the MPU9250 gyroscope and QMC5883P magnetic heading sensor onboard the FWR, which can accurately measure the azimuth angle of the FWR MAV. Since the FWR MAV is constantly flying in a spinning state, its fuselage azimuth angle is equivalent to the azimuth angle of the rotor. This azimuth angle $\psi$ can be utilized for virtual cyclic pitch control:

$$\begin{cases} \varphi_R = \varphi + A_R \sin(\psi) + A_P \sin(\psi - \frac{\pi}{2}) \\ \varphi_L = \varphi + A_R \sin(\pi + \psi) + A_P \sin(\psi + \frac{\pi}{2}) \end{cases} \tag{41}$$

In the above formula, $\varphi$ is the imitation dragonfly pitching angle calculated by the Eq.(6) .$\varphi_R$ and $\varphi_L$ are the output angles of left-wing servo and right-wing servo, $\psi$ is the rotor azimuth angle measured by the magnetic heading sensor, $A_p$ and $A_r$ are the cycle pitch amplitude in the roll direction and pitch direction. When $A_p$ and $A_r$ are adjusted, the control torque output in the direction of pitch axis and roll axis can be realized.

Undoubtedly, the values of $A_p$ and $A_r$ are instrumental in gauging the rotor's efficiency and the efficacy of attitude control. Excessively large values lead to a pronounced increase in the blade element's angle of attack $a_*$, subsequently diminishing the rotor's lift efficiency. In contrast, overly small values might render the rotor incapable of producing adequate control torque, compromising the FWR's attitude adjustment capabilities.

Therefore, the judicious selection of $A_p$ and $A_r$ values is paramount. The challenge lies in achieving a harmonious equilibrium where the rotor can produce ample attitude control force without compromising efficiency. Their optimization ensures that the FWR exercises meticulous control over its attitude, facilitating fluid flight manoeuvres, efficient lift production, and exemplary performance across diverse flight scenarios.

To delve deeper into this matter, both a Simulink experiment (grounded in the mathematical model presented in Chapter 4) and a hands-on platform experiment were undertaken. These aimed to discern the optimal $A_p$ and $A_r$ values. As a foundational step in this exploration, it's imperative to delineate the efficiency parameters of the FWR.

According to literature (Ref.15), the aerodynamics Power efficiency of FWR is defined as:

(42) $$P_f = \frac{\bar{C}_l}{\bar{C}_l - \bar{C}_d}$$

Where, $\bar{C}_l$ is the average lift coefficient of the whole wing, and $\bar{C}_d$ is the average lift coefficient of the whole wing.

Furthermore, according to literature (Ref.15), we have power efficiency:

(43) $$S_P = \frac{L}{P}$$

Among these parameters, $L$ represents the lift generated by the FWR (in Newtons), and $P$ represents the input power to the FWR motor (in Watts). For this research, a constant flapping frequency of 15Hz was utilized. This study focused on varying the pitch amplitude (AMP) from 0° to 40° while examining their effects on efficiency, rotor speed, and blade angle of attack on an experimental platform，the results are as follow Figure.

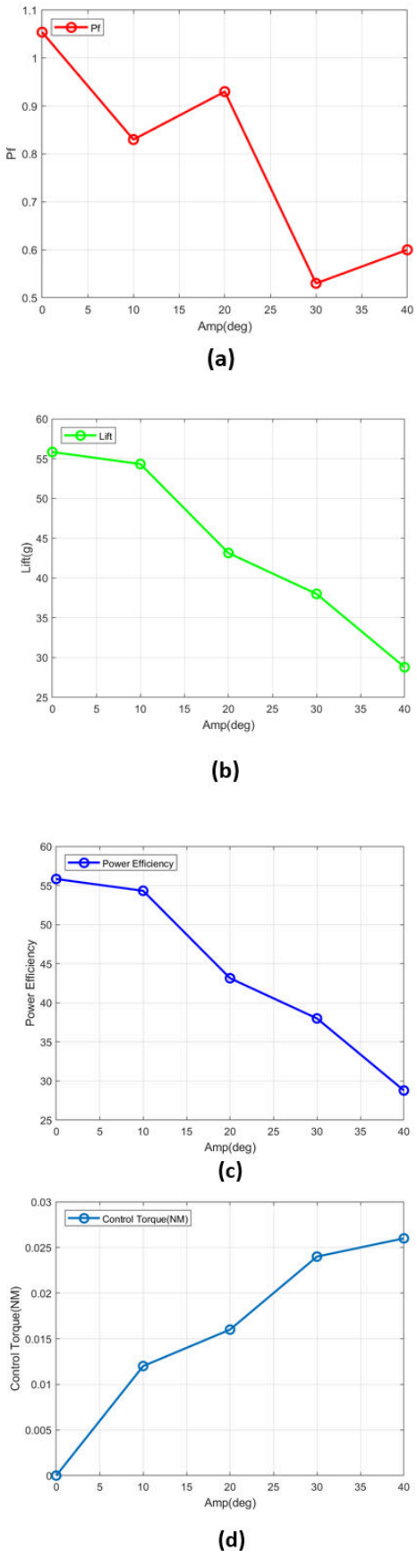


Figure 14 The Effect of Pitch Amplitude on Efficiency

As shown in the Figure 14 above, when the rotor cycle pitch amplitude(Amp) increases, the aerodynamic efficiency decreases stepwise. Different from the declining trend of power supply efficiency in Figure 14-c, the aerodynamic efficiency $P_f$ (Figure 14-a) drops most obviously when the amplitude ranges from 20° to 30°, and the decline rate of aerodynamic efficiency becomes flat from 30° to 40°.

In terms of lift (Figure 14-b), as the Amp increases, the lift drops significantly from 55.83g to 28.79g. The control torque exhibits a continuous increase as the amplitude (Amp) value increases, and the maximum control torque value reaches 0.026NM.

The weight of FWR is 30g, therefore, the result of cyclic pitch cannot make its lift less than it. On the other hand, since the rotor rotates passively, increasing Amp will decrease $\Omega$ the passive rotation of the rotor, which in turn will affect the frequency of cyclic control.

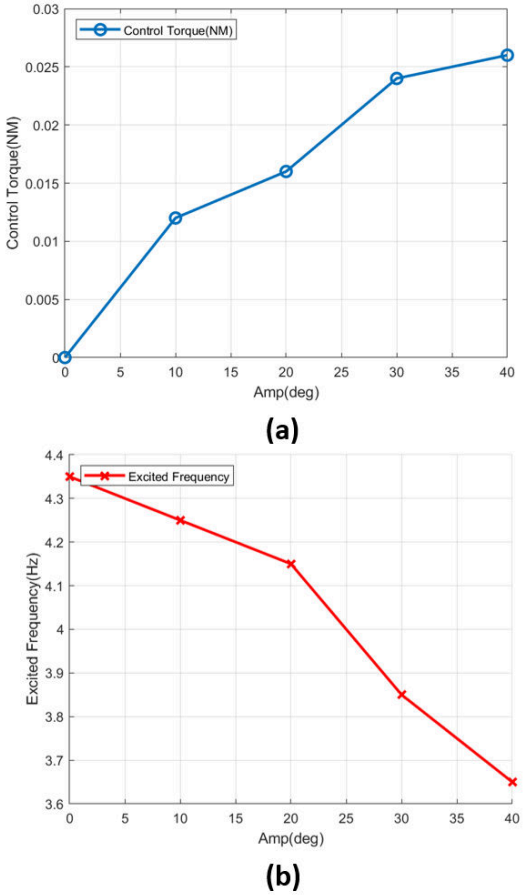


Figure 15 The relationship between AMP and Control torque, Control frequency

The Figure 15 above illustrates the relationship between the control torque generated by cyclic control and the control frequency. As the amplitude (AMP) increases, the control frequency decreases while control torque increases.

Based on the design index, the FWR MAV needs to be capable of carrying at least 15g of load weight in addition to its 30g self-weight, resulting in a Maximum Take-off Weight (MTOW) of 45g. Considering this requirement, we can select the flight parameters that are suitable for the FWR MAV's Minimum Flight Weight (MFW) and MTOW from the above calculations as follows:

Table 5 Typical Flight Parameters of FWR

| Parameters | MFW(30g) | MTOW(30g+15g=45g) |
|---|---|---|
| **Amp** | 30 | 10 |
| **Pf** | 0.53 | 0.83 |
| **Power Efficiency** | 0.027 | 0.037 |
| **Control Torque(NM)** | 0.024 | 0.012 |
| **Lift(g)** | 38 | 54.32 |
| **RPS** | 7.7 | 8.5 |
| **Control Freq(Hz)** | 3.85 | 4.25 |

From the data presented in the preceding table, it becomes clear that an escalation in system load necessitates a decrement in control torque. As this control torque diminishes, both the aerodynamic efficiency and power efficiency of the system see enhancements. Nonetheless, striking the optimal equilibrium is vital; an overly reduced control torque could jeopardize the aircraft's flight stability. The methodology to harmonize control torque, load, and stability remains a subject of ongoing research, and as of this paper's conclusion, the investigation remains unfinished.

## 7. CONCLUSIONS

In this article, a new mathematical model for FWR MAV has been proposed. The model utilizes a new experiments-based correction method to accurately calculate the proportion of steady and unsteady aerodynamic forces. Compared to previous models such as H. Li and S. Guo's model, which only accounted for low flapping frequencies under 10Hz (RMSE=43.73), and Kirchhoff and Helmholtz model, which did not consider the low Reynolds number effects (RMSE=14.72), our mathematical model demonstrates significant improvement, achieving an

RMSE of 5.22. Notably, our model takes into account the full flapping frequency range of FWR MAV, ranging from 0-20Hz, and also considers the effects of low Reynolds numbers. Through this research, we have made significant strides towards improving the understanding and modelling of FWR MAV's flight dynamics, contributing to the development of more efficient and capable Micro Air Vehicles in the future. However, further validation and refinement are still required to optimize the model's performance and applicability in various scenarios.

## 8. REFERENCES


1. Bao XQ, Bontemps A, Grondel S, Cattan E. Design and fabrication of insect-inspired composite wings for MAV application using MEMS technology. Journal of Micromechanics and Microengineering. 2011 Dec 1;21(12):125020.

2. Ward TA, Fearday CJ, Salami E, Binti Soin N. A bibliometric review of progress in micro air vehicle research. International Journal of Micro Air Vehicles. 2017 Jun 2;9(2):146–65.

3. Gerdes JW, Gupta SK, Wilkerson SA. A Review of Bird-Inspired Flapping Wing Miniature Air Vehicle Designs. J Mech Robot. 2012 May 1;4(2).

4. TAYLOR GK. Mechanics and aerodynamics of insect flight control. Biological Reviews. 2001 Nov;76(4):449–71.

5. Phan HV, Aurecianus S, Au TKL, Kang T, Park HC. Towards the Long-Endurance Flight of an Insect-Inspired, Tailless, Two-Winged, Flapping-Wing Flying Robot. IEEE Robot Autom Lett. 2020 Oct;5(4):5059–66.

6. Li H, Guo S, Zhang YL, Zhou C, Wu JH. Unsteady aerodynamic and optimal kinematic analysis of a micro flapping wing rotor. Aerosp Sci Technol. 2017 Apr 1;63:167–78.

7. Guo S, Yang D, Lal Kummari K, Huang Z. A Smart Material Flapping Wing Micro Rotorcraft Back to Programme Back to Topic.

8. Li H, Guo S. Aerodynamic efficiency of a bioinspired flapping wing rotor at low reynolds number. R Soc Open Sci. 2018 Mar 14;5(3).

9. Guo S, Li H, Zhou C, Zhang YL, He Y, Wu JH. Analysis and experiment of a bio-inspired flyable micro flapping wing rotor. Aerosp Sci Technol. 2018 Aug;79:506–17.

10. Wan J, Pavel MD. Designing the Ornicopter, a tailless helicopter with active flapping blades: a case study. Proc Inst Mech Eng G J Aerosp Eng. 2016 Oct 8;230(12):2195–219.

11. de Croon GCHE, de Clercq KME, Ruijsink R, Remes B, de Wagter C. Design, Aerodynamics, and Vision-Based Control of the DelFly. International Journal of Micro Air Vehicles. 2009 Jun 1;1(2):71–97.

12. Guo S, Li H, Zhou C, Zhang YL, He Y, Wu JH. Analysis and experiment of a bio-inspired flyable micro flapping wing rotor. Aerosp Sci Technol. 2018 Aug 1;79:506–17.

13. Wang ZJ. DISSECTING INSECT FLIGHT. Annu Rev Fluid Mech. 2005 Jan 1;37(1):183–210.

14. Chen L, Zhang Y, Zhou C, Wu J. Aerodynamic mechanisms in bio-inspired micro air vehicles: a review in the light of novel compound layouts. IET Cyber-Systems and Robotics. 2019 Jun 4;1(1):2–12.

15. Li H, Guo S. Aerodynamic efficiency of a bioinspired flapping wing rotor at low Reynolds number. R Soc Open Sci. 2018 Mar 14;5(3):171307.

16. Chen S, Wang L, He Y, Tong M, Pan Y, Ji B, et al. Aerodynamic Performance of a Flyable Flapping Wing Rotor With Passive Pitching Angle Variation. IEEE Transactions on Industrial Electronics. 2022 Sep 1;69(9):9176–84.

17. Guo S, Li D, Wu J. Theoretical and experimental study of a piezoelectric flapping wing rotor for micro aerial vehicle. Aerosp Sci Technol. 2012 Dec;23(1):429–38.

18. Keennon M, Klingebiel K, Won H. Development of the Nano Hummingbird: A Tailless Flapping Wing Micro Air Vehicle. In: 50th AIAA Aerospace Sciences Meeting including the New Horizons Forum and Aerospace Exposition. Reston, Virigina:

American Institute of Aeronautics and Astronautics; 2012.

19. Phan HV, Park HC. Remotely controlled flight of an insect-like tailless Flapping-wing Micro Air Vehicle. In: 2015 12th International Conference on Ubiquitous Robots and Ambient Intelligence (URAI). IEEE; 2015. p. 315–7.

20. Phan HV, Aurecianus S, Kang T, Park HC. KUBeetle-S: An insect-like, tailless, hover-capable robot that can fly with a low-torque control mechanism. International Journal of Micro Air Vehicles. 2019 Jan 15;11:175682931986137.

21. Tu Z, Fei F, Deng X. Untethered Flight of an At-Scale Dual-motor Hummingbird Robot with Bio-inspired Decoupled Wings. IEEE Robot Autom Lett. 2020;1–1.

22. Zhang J, Tu Z, Fei F, Deng X. Geometric flight control of a hovering robotic hummingbird. In: 2017 IEEE International Conference on Robotics and Automation (ICRA). IEEE; 2017. p. 5415–21.

23. Zhang T, Zhou C, Su S. Design and development of bio-inspired flapping wing aerial vehicles. In: 2015 International Conference on Advanced Robotics and Intelligent Systems (ARIS). IEEE; 2015. p. 1–6.

24. Teoh ZE, Fuller SB, Chirarattananon P, Prez-Arancibia NO, Greenberg JD, Wood RJ. A hovering flapping-wing microrobot with altitude control and passive upright stability. In: 2012 IEEE/RSJ International Conference on Intelligent Robots and Systems. IEEE; 2012. p. 3209–16.

25. Padfield GD. Helicopter flight dynamics: the theory and application of flying qualities and simulation modelling. John Wiley & Sons; 2008.

26. Chen S, Li H, Guo S, Tong M, Ji B. Unsteady aerodynamic model of flexible flapping wing. Aerosp Sci Technol. 2018 Sep;80:354–67.

27. Gursul I, Wang Z, Vardaki E. Review of flow control mechanisms of leading-edge vortices. Progress in Aerospace Sciences. 2007 Oct;43(7–8):246–70.

28. Wang ZJ, Birch JM, Dickinson MH. Unsteady forces and flows in low Reynolds number hovering flight:two-dimensional computations *vs* robotic wing experiments. Journal of Experimental Biology. 2004 Jan 22;207(3):449–60.

29. Wang H, Zeng L, Liu H, Yin C. Measuring wing kinematics, flight trajectory and body attitude during forward flight and turning maneuvers in dragonflies. Journal of Experimental Biology. 2003 Feb 15;206(4):745–57.

30. Truong QT, Nguyen Q V, Truong VT, Park HC, Byun DY, Goo NS. A modified blade element theory for estimation of forces generated by a beetle-mimicking flapping wing system. Bioinspir Biomim. 2011 Sep 1;6(3):036008.

31. M. B. Tischler et al. Rotorcraft Flight Simulation Model Fidelity Improvement and Assessment. North Atlantic Treaty Organization,. 2021 May;

32. Lu L, Agarwal D, Padfield GD, White MD, Cameron N. A New Heuristic Approach to Rotorcraft System Identification. Journal of the American Helicopter Society. 2023 Apr 1;68(2):42–58.

33. Lu L, Padfield GD, White M, Perfect P. Fidelity enhancement of a rotorcraft simulation model through system identification. The Aeronautical Journal. 2011 Aug 27;115(1170):453–70.

## 9. CLASSIFICATION & COPYRIGHT

accessible web-based repository 2 years after the respective conference.

2023-09-07

# Modelling and simulation of a novel bioinspired flapping-wing rotary MAV

Huang, Xun

German Society for Aeronautics and Astronautics (DGLR: Deutsche Gesellschaft für Luft- und Raumfahrt)

Huang X, Lu L, Whidborne J, Guo S. (2023) Modelling and simulation of a novel bioinspired flapping-wing rotary MAV. In: 49th European Rotorcraft Forum (ERF49 2023), 5-7 September 2023, Bückeburg, Germany

https://erf2023.dglr.de/